Fine structure of excitons and electron–hole exchange energy in polymorphic CsPbBr 3 single nanocrystals

Julien Ramade, Léon Marcel Andriambariarijaona, Violette Steinmetz, Nicolas Goubet, Laurent Legrand, Thierry Barisien, Frédérick Bernardot, Christophe Testelin, Emmanuel Lhuillier, Alberto Bramati, et al.

Fine Structure of Excitons and electron-hole exchange energy in Polymorphic $CsPbBr_3$ Single Nanocrystals

Julien Ramade[a], Léon Marcel Andriambariarijaona[a], Violette Steinmetz[a], Nicolas Goubet[a], Laurent Legrand[a], Thierry Barisien[a]*, Frédérick Bernardot[a], Christophe Testelin[a], Emmanuel Lhuillier[a], Alberto Bramati[b], Maria Chamarro[a].

All inorganic $CsPbX_3$ (X = Cl, Br, I) nanocrystals (NCs) belong to the novel class of confined metal-halide perovskites which currently arouses enthusiasm and stimulates a huge activity due to outstanding properties across several fields of optoelectronics. A deep knowledge of the band-edge excitonic properties in those materials is thus crucial to further optimize their performances. Here, high-resolution photoluminescence (PL) spectroscopy of single bromide-based NCs reveals the exciton fine structure under the form of sharp peaks linearly polarized and grouped in doublet or triplet, which directly mirror the adopted crystalline structure, tetragonal (D_{4h} symmetry) or orthorhombic (D_{2h} symmetry). Intelligible equations are found that show how the fundamental parameters (spin-orbit coupling, Δ_{SO}, crystal field term, T, and electron-hole exchange energy, J) rule the energy spacings in doublets and triplets. From experimental data, fine estimations of each parameter are obtained. The analysis of the absorption spectra of an ensemble of NCs with a "quasi-bulk" behavior leads to Δ_{SO} = 1.20 ± 0.06 eV and T = - 0.34 ± 0.05 eV in $CsPbBr_3$. The study of NCs individual luminescence responses having sizes comparable to the exciton Bohr diameter, 7 nm, allows us to estimate the value of J around ≈ 3 meV in both tetragonal and orthorhombic phases. This value is already enhanced by confinement.

Introduction

The highly efficient and low-cost photovoltaic devices obtained from hybrid organic-inorganic perovskites have fueled a strong interest in perovskite semiconductors.[1–3] Notably, confined structures - from 0D to 2D - of the novel inorganic Cesium family ($CsPbX_3$, X = Cl, Br, I) obtained through colloidal synthesis have recently emerged as a new class of nanomaterials with exceptional optical properties.[4–6] The photoluminescence (PL) properties of nanocrystals (NCs) - essentially 0D - have been mostly investigated with the demonstration of a large absorption cross-section,[7] high tunability through band-gap engineering (by complete or partial replacement of the halide anion) and quasi-unitary room-temperature emission yields.[5] Their outstanding optoelectronic performances, which outclass the performances of II-VI semiconductors counterparts,[8,9] result from a high defect tolerance in terms of electronic structure.[9,10] Inorganic perovskite NCs also benefit from improved thermal and photo-stabilities.[8] Far advanced studies have confirmed lead-halide perovskite NCs as a high-gain medium with a wide potential for room-temperature (RT) photonic applications: low- threshold amplified spontaneous emission and random lasing of emitters coupled to spherical resonators[11] or two-photon-pumped lasing.[7] In addition, quantum regimes of 0D emitters with a reduced emission blinking were evidenced.[12–15]

$CsPbX_3$ perovskites are direct bandgap semiconductors. They adopt different crystalline structures determined by the temperature and the nature of their growth processes.[1] Their bulk band structure was determined in early calculation[16,17] and regularly upgraded.[18–20] The band-edge excitons of halide perovskite are Coulomb bound states, pairing a hole in the upper valence band (S = 1/2, $S_z = \pm 1/2$) and an electron from the lowest split-off band (J=1/2, $J_z=\pm1/2$). For orthorhombic (tetragonal) crystal structures, the electron-hole exchange interaction and the crystal field terms split the 4-fold degenerated bulk band-edge exciton into four (three) levels with an optically forbidden exciton state at lowest energy.[21] For NCs with size comparable or smaller than the Bohr diameter, the electronic quantum confinement modifies the electronic density of states leading to a discretization of the whole spectrum, and is also at the origin of a blue-shift of the band-edge for decreasing NC size. The electron-hole exchange interaction is proportional to the spatial overlap of the electron and hole wave-functions. A sharp enhancement of the electron-hole exchange energy due to the electronic confinement has been already demonstrated in low-dimensional systems.[22–26]**.** Moreover the anisotropy of the confinement potential, mainly fixed by the NC shape, can lead to a fine exciton structure deeply different from the bulk fine structure of the material.[27,28] Reduction of the orthorhombic or tetragonal symmetries by Rashba effects can also be at the origin of a forbidden exciton state at highest energy or produce a four bright states manifold.[29]

A detailed understanding of the band-edge exciton states is of prime importance to explain the outstanding optical properties of inorganic perovskite NCs and to explore their applications in nanophotonics and quantum optics or quantum information devices. The polarization directions of the emitted photons,[30] selection rules in absorption and emission are the basic parameters which come into play. More crucially, the exciton manifold offers a model platform to implement quantum manipulation processes,[31,32] and the exciton energy-level splitting or fine structure (FS) splitting is also a crucial parameter from the point of view of entangled photons generation, the maximization of the entanglement requiring that the FS splitting energy remains lower than the radiative linewidth.[33,34] FS splitting also pilots the temperature dependence of both the dynamics and efficiency of the NC emission, in particular through the thermal equilibrium which is established in the manifold and a possible exciton storage in optically dark states.[35] The knowledge of the FS thus paves the way to accurate models for intrinsic excitonic responses, and allows disentangling the various pathways that govern energy relaxation in NCs.

Here, we present a quantitative study of the band-edge exciton FS of single $CsPbBr_3$ NCs with sizes comparable to the Bohr diameter, $2a_B \approx 7$ nm. The polarization analysis of the low-temperature micro-luminescence (μ-PL) confirms the existence of two characteristic FSS of bright exciton states - doublet and triplet – which are respectively associated to the responses of individual NCs with tetragonal and orthorhombic crystalline structures.[21] The signature of a high-symmetry cubic phase is not observed in our experiments. Following a perturbative approach based on the derivation proposed by Fu et *al.*,[21] we demonstrate that the FS splitting in orthorhombic crystals is a function of the spin-orbit coupling parameter, crystal-field term and electron-hole exchange interaction, as in tetragonal perovskites. Explicit equations that connect those parameters are derived. The tetragonal spin-orbit coupling and crystal field are extracted from the absorption

spectra of an ensemble of "quasi-bulk" NCs. Experimental μ-PL spectra of single NCs provide the energy differences (between peaks in doublets and triplets) which, through the previous equations, lead to the estimation of the electron-hole exchange energy, *J*, associated to the band-edge $CsPbBr_3$ exciton. We find a value $J \approx 3$ meV for both structures that does not change within the explored NC size range but that is clearly affected by the electronic confinement. Our analysis also provide the absolute value of the additional orthorhombic crystal field contribution, $|\varepsilon|$, with respect to the tetragonal one ($|\varepsilon| \approx 0.08$ eV).

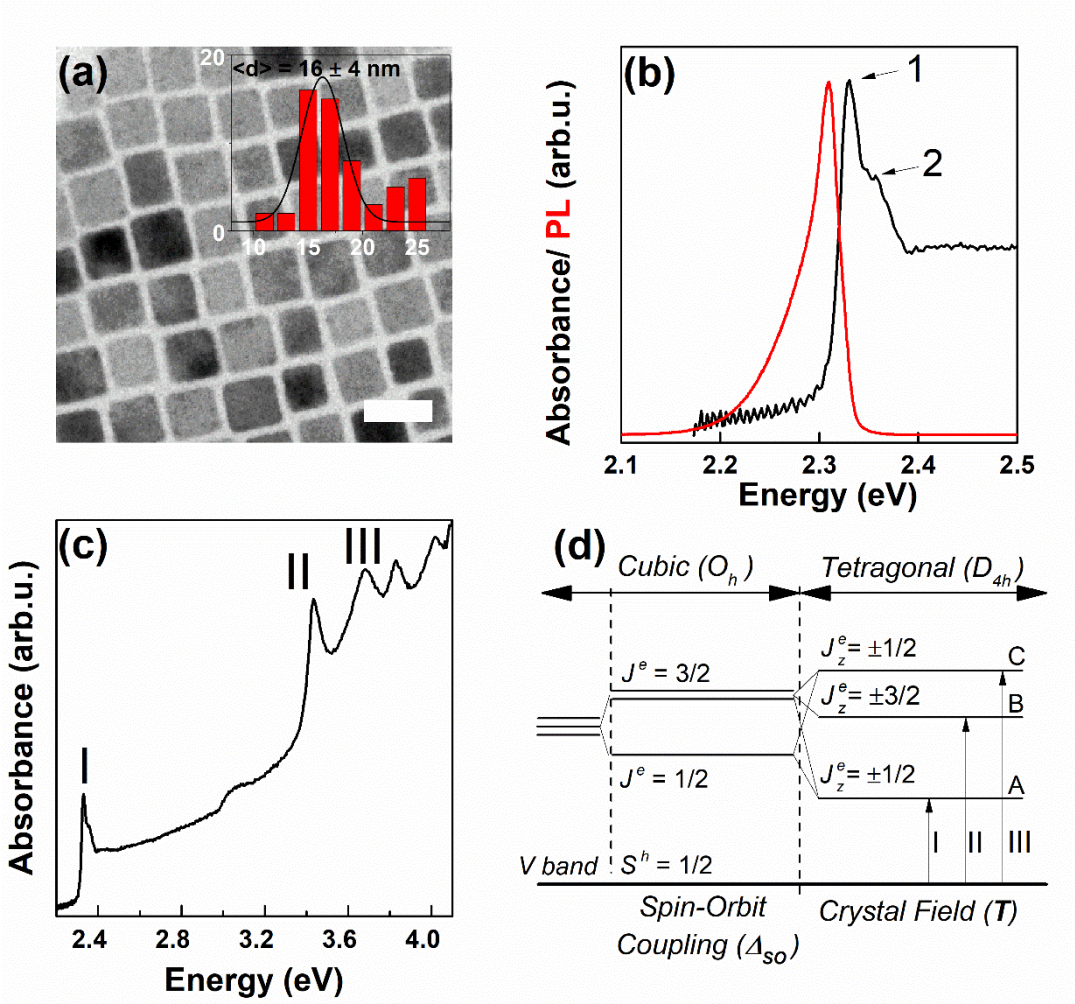

Figure 1: (a) TEM image of NCs synthesized at 180 °C (sample 1). The scale bar corresponds to 20 nm. Inset: size distribution in the sample. (b) Absorption (black) and luminescence (red) spectra of the same sample in the low-energy range, at 11 K. (c) Entire absorption spectrum at 11 K. (d) Scheme of the band structure evolution in perovskite NCs from the high-symmetry (cubic) phase to the lower-symmetry tetragonal phase under the effect of Spin-Orbit coupling and crystal field. The upper valence band (denoted as V band) states are denoted ($S^h = \frac{1}{2}$, $S_z^h = \pm\frac{1}{2}$). In tetragonal NCs, three degenerate levels (A, B and C) compose the excited manifold ($J^e = \frac{1}{2}$, $J_z^e = \pm\frac{1}{2}$), ($J^e = \frac{3}{2}$, $J_z^e = \pm\frac{3}{2}$) and ($J^e = \frac{3}{2}$, $J_z^e = \pm\frac{1}{2}$). S_z^h - J_z^e - are the z components of the total hole - electron - angular momentum S^h - J^e.

Experimental methods

Chemical synthesis of $CsPbBr_3$ NCs is presented in detail in the Electronic Supplementary Information (ESI). For structural characterization through transmission electron microscopy, the prepared solution was diluted and a drop was deposited for impregnation on a microscopic grid. Samples elaborated for spectroscopic measurements consisted of a spin-coated deposited drop of a diluted solution onto a glass slide. Transmission electron microscopy observations were performed with a JEOL-2010F working at 200 kV. X-ray diffraction patterns were performed with a Philips X' pert operated at 40 kV and under 40 mA, using the Cu Kα line (wavelength 1.54 Å).

Optical transmission spectra were measured using a CARY 5000 double-beam spectrophotometer (Varian company) with a 4 Å resolution. For temperature-dependent studies, a commercial helium exchange gas cryostat was used. The temperature was monitored between ≈ 11 K

and ambient temperature by Si diodes and controlled by heating of the gas. μ-PL experiments were carried out as a function of temperature using a confocal-like microscope. For this study, we worked mainly with an Ar continuous wave laser emitting at 475 nm, with an average excitation power of 2.5 μW on a spot of ≈ 1.5 μm in diameter. The excitation laser beam is focused using a microscope objective with NA = 0.6. The samples are mounted on the cold finger of a μ-PL cryostat (Oxford Instruments) designed to compensate for thermal expansion and to keep spatial position of the spot as temperature is changed. The luminescence collected with the same objective is analyzed in an ACTON SP2760i Roper Scientific-Princeton Instruments spectrometer coupled to a nitrogen-cooled SPEC10 (RS-PI) CCD camera, with an overall spectral resolution of 50 μeV. The objective located outside the cryostat is attached to a three-axes piezo stage, allowing to finely scan the sample. Polarization measurements were performed by adding a motorized half-wave plate followed by an analyzer (the direction of which is parallel to the grating grooves in order to obtain the largest response) placed at the spectrometer entrance.

Results and discussion

Figure 1a shows a representative transmission electron microscopy (TEM) performed on sample 1, grown at 180 °C. NCs present a cubic shape whose size follows a Gaussian distribution centered at 16 nm with a full width at half maximum (FWHM) of 4 nm (see inset of Figure 1a**).** At 11 K, the first absorption peak (Figure 1b, black spectrum) is located at 2.33 eV (indexed as 1) and is characterized by a shoulder on the high-energy side, at 2.36 eV (indexed as 2). Both features have been interpreted in bulk materials as the 1S and 2S excitons, respectively.[17]

The energy difference between these two peaks is equal to 30 meV and allows to experimentally estimate the exciton binding energy (EBE) to 40 meV. EBE is a very important parameter for evaluating light-emitting efficiencies and confinement effects in perovskite materials (see below). From the classical formula which connect the EBE value to the exciton Bohr radius, a_B, and injecting the calculated values of the effective mass for electrons and holes for $CsPbBr_3$ ($m_e \approx m_h \approx 0.15$ in units of electron mass[5]), we find $a_B \approx 3.5$ nm. In the high-energy range of Figure 1c, we also observe a second sharp peak (denoted II) at 3.44 eV and a group of three peaks at 3.68 (denoted III), 3.83 and 4.01 eV. These energies compare well with peaks observed in bulk $CsPbBr_3$ crystals.[16,17] 11 K macro-photoluminescence (PL, red spectrum in Figure 1b) presents a Stokes-shifted peak at 2.31 eV related with exciton emission, and a low-energy tail which is more clearly related to defects or/and phonon replica emission. We also observe an "anomalous" temperature behavior of the peaks in the absorption and luminescence spectra, *i.e.* a blue shift accompanied by a broadening of the peaks with increasing temperature (see ESI, Figure S2). The first absorption peak increases in energy as the temperature increases, from 2.33 eV at 11 K to 2.38 eV at 290 K. This behavior has already been observed in $CsPbBr_3$ bulk[36] and nanocrystals,[37] and in other hybrid perovskites.[38] It is discussed in detail in the ESI section (Figure S3). As the described spectral features clearly suggest, excitons in sample 1 have a bulk-like behavior. From the absorption spectrum and the calculation derived by Yu in analogous low-symmetry bulk hybrid perovskites, we obtain the crystal field correction with respect to the cubic phase, T, and the amplitude of the spin-orbit interaction in $CsPbBr_3$ through the spin-orbit coupling parameter, Δ_{SO}.[20] Both parameters fundamentally characterize the electronic band structure and, to a larger extent, determine the exciton fine structure discussed in the next paragraphs. We therefore associate the three peaks located at 2.33, 3.44 and 3.68 eV, denoted I, II and III in the absorption spectrum of sample 1 (Figure 1c), to optical transitions between the top of the valence band to the bottom of three bands (A, B and C) whose states result from a partial lifting of degeneracy in the electronic states of the cubic structure (see Figure 1d). The shoulder observed in the absorption spectra at 3.05 eV was identified in bulk material as due to a van-Hove singularity at the point M of the Brillouin zone.[17] Using the values of the three positions in energy, we finally obtain (see ESI) $\Delta_{SO} = 1.20 \pm 0.06$ eV and $T = -0.34 \pm 0.05$ eV, which are characteristic values in Pb-based compounds. [20,39] We further assert that these extracted values are poorly influenced by the NC crystalline structure (tetragonal or orthorhombic) as well as by the approximation consisting in assimilating excitonic and band-to band transitions (see developed justification in ESI).

For sufficiently small sizes, the concerted effect of polydispersity and confinement leads to the splitting in energy of the excitonic transitions. This "spectral dilution" adds to spatial dispersion and makes easier the process which consists in isolating single NC responses in a high-resolution micro-spectroscopy configuration. To that purpose, a highly polydisperse sample was elaborated (sample 2). Synthesis at much lower temperature (110 °C) still provides cubic-shaped NCs (see ESI, Figure S1a); however sizes now range from 5 nm to 23 nm, with an average size of 12.5 nm and a FWHM of 11.5 nm **(**see ESI, Figure S1b). Figure 2a contains low-temperature absorption and PL spectra of sample 2 in the range 2.10 eV to 2.55 eV. Two important features should be emphasized: both spectra show more structures than the corresponding ones for sample 1, and the majority of structures are blue-shifted. Moreover, the PL peaks are slightly Stokes-shifted (≈ 20 meV) from the corresponding absorption peaks. The temperature dependence of these absorption and PL peaks follows a similar behavior to the one of the energy gap in perovskite bulk materials (see Figure 2b and ESI, Figure S4). We come to the conclusion that at least the three high-energy structures in absorption which share the same behaviors (as well as their images in PL) correspond to the responses of different sub-populations present in the original NCs size distribution. Let us note that the lowest absorption peak (reversed black filled triangle) and the second lowest PL peak (black filled triangle) do not share the same features and will not be further considered. The lowest energy PL band is red-shifted by ≈ 60 meV compared to the lowest absorption peak and is then more probably related with defects than to an intrinsic transition. In the used pulsed regime, with a mean excitation power of a few μW, and according to the one-photon absorption cross section in the system (an upper value, $\sigma \approx 10^{-13}$ cm^2, was considered)[5,7,40], no more than one electron-hole pair is created in a single NC so that non-linear effects in the emission may be discarded. Then PL peaks observed at higher energy than 2.33 eV are clearly associated to NCs with sizes comparable or smaller than the bulk Bohr diameter. A rough estimation of the expected blue-shift is obtained - for the sake of simplicity - by considering the limit situation of strong confinement. Using the expression $\Delta E_c = (3\hbar^2\pi^2/2\mu d^2)$ for the confinement energy in a cubic box (with d, the length dimension of the NC cube, and $\mu = 1/(m_e^{-1}+m_h^{-1})$, the exciton reduced mass in free electron mass units), and neglecting Coulombic effects, we find, for $d = 2a_B \approx 7$ nm, a value of the excitonic transition $E_g + \Delta E_c \approx 2.6$ eV. Whether slightly overestimated, the result is globally consistent with the displacement of the absorption observed in sample 2. A good agreement for our estimation of the

NC size - energy relationship is also found with studies which addressed the size dependence of the NC band gap when taking into account the increase of the gap with the temperature.[5,41]

In order to gain insights into the intrinsic properties of these $CsPbBr_3$ NCs, low-temperature μ-PL experiments were finally performed on highly-diluted phases generated from sample 2, which possesses the highest polydispersity. Experiments were carried out using a home-made microscope (see details in the ESI). Globally, 20 individual objects were studied; eleven of them present an excitonic FS composed of a set of three peaks (upper spectrum of Figure 3a) adopting a Lorentzian profile with narrow linewidths between 0.2 and 0.7 meV, and an energy spacing between two consecutive peaks varying from 0.2 to 0.9 meV (see ESI, Table S1). Another FS was detected, namely a doublet-like excitonic band (Figure 3b, upper spectrum) where in first approximation, peaks possess comparable energy spacings and linewidths. To initiate the interpretation, we will conform with the analysis made by Fu *et al.*[21] where connections are established between the excitonic FS

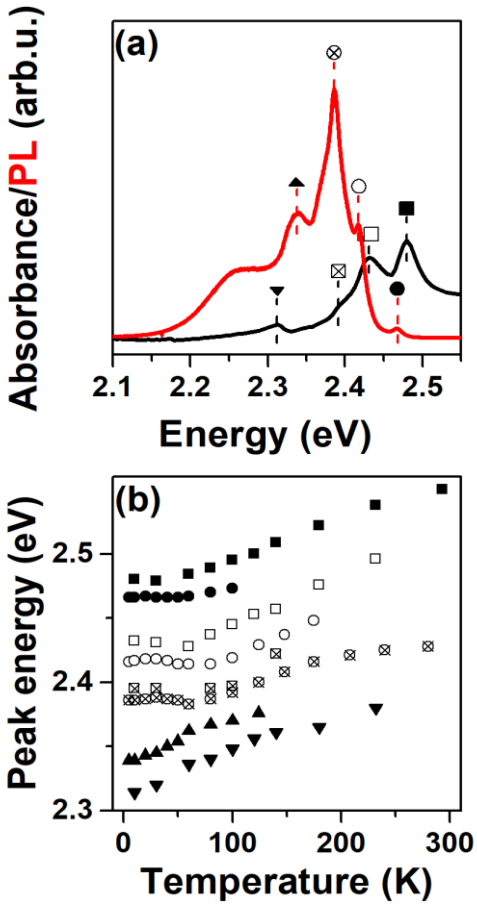

Figure 2: (a) Absorption (black) and emission (red) spectra of sample 2 at 11 K. Squares and circles with the same patterns denote the absorption and luminescence of the same level. Filled triangles represent absorption and luminescence peaks which do not correspond to the same level. (b) Evolution of both absorption and emission peak positions with temperature.

and symmetry properties of the unit cell. Two structures are likely to coexist in our sample: the orthorhombic one which is found stable at low temperature,[42,43] and the tetragonal one, possibly stabilized by the fast cooling applied to the mixture during the synthesis. Lowering the symmetry from the tetragonal to the orthorhombic phase affects the band diagram very slightly (see ESI); inversely that strongly affects the band-edge exciton structure for an exciton composed of a hole $S^h = \frac{1}{2}$, $J_z^h = \pm\frac{1}{2}$ and an electron from the lowest $J^e = \frac{1}{2}$, $J_z^e = \pm\frac{1}{2}$ conduction band. For tetragonal NCs, it is expected that the lowest level, $|0_D\rangle$, is optically inactive, and followed with increasing energy by a linearly polarized bright state, $|0_B\rangle$, and two-fold degenerate circularly-polarized bright states, $|\pm1\rangle$. In the orthorhombic structure, the upper

degenerate states split, revealing a three-bright-states FS with crossed linear polarizations (denoted |X>, |Y> and |Z>, where |X> and |Y> refer to the split states - see Figures 3c and 3d).

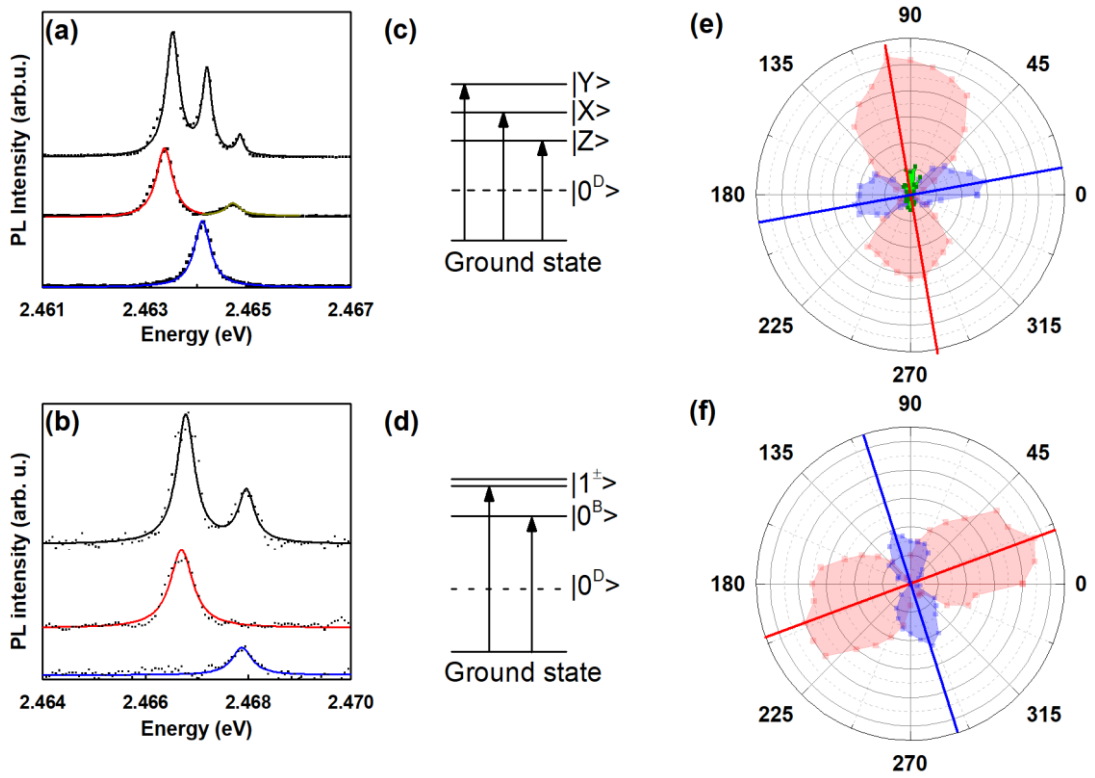

Figure 3: μ-PL of two individual NCs at 5 K. (a) Typical triplet and (b) doublet measured with an excitation power in the μW range. The upper spectra were measured without analyser. The middle and lower spectra were measured with an analyser oriented along the respective polarization of each peak. Experimental data were fitted with multiple (two or three) or single Lorentzian functions. (c-d) Representative schemes of the exciton fine structure for $CsPbBr_3$, orthorhombic (c), and tetragonal, (d), phases. Polarization diagrams are for the shown triplet (e) and doublet (f). Blue and red solid lines show the polarization axis of each peak.

To probe these theoretical predictions, the polarization of each PL peak was analyzed using a linear polarizer and a motorized half-wave plate whose one neutral axis makes an angle φ with the transmission axis of the linear polarizer. Thanks to the great PL stability (see ESI, Figure S6), a polarization diagram is built for each studied structure, each point representing the integrated intensity of one peak at a given orientation of the half-wave plate, from φ = 0° to φ = 180°, with respect to the linear polarizer (see, for instance, Figures 3e and 3f which characterize a triplet and a doublet, respectively).

The results concerning triplets are unambiguous and will be described first. In triplets, two peaks present linear and crossed polarizations, and are accompanied by a third peak of much lower amplitude and whose polarization is less well defined. Figure 3a shows such a configuration. This is clearly in agreement with the theoretical scheme. The PL response of the peak associated to the state for which the polarization direction is aligned with the setup detection axis, should ideally not be detectable; however, slight NC misalignments and PL light measured in the angle of acceptance of the objective allow its manifestation. In our experiments, several configurations were observed with a distribution in intensity varying in the triplet from one NC to the other, which were associated to different NC orientations. It is thus globally difficult to disentangle geometric effects from thermal occupation effects to explain the relative weights of the peaks in the spectra. However, when two equivalent - *i.e.*, having their polarizations orthogonal in the sample plane - states are detected (case depicted in Figure 3a) one finds ratios in their integrated amplitudes fully coherent with populations imposed by the Boltzmann distribution. Within this study, polarization measurements performed on doublets reveal exclusively two linear and perpendicular lines (Figure 3b, middle and lower spectra and Figure 3f). Such a configuration is compatible with crystals having their **c** axis in the plane of the sample. To the lowest energy $|0^B\rangle$ state is indeed associated a dipole polarized along **c**. As NCs lay down flat on the substrate with one of their crystallographic facet parallel to the substrate surface, our polarizer will probe this direction but will also select the component of the field in the plane perpendicular to **c** (which contains the "detection" direction). It is moreover striking that the energy separation between both components of doublets is in average markedly higher than any of the energy distances between the peaks in triplets (Figure 4a and ESI, Table S1). Let us note that the measurements with long integration times do not show any hints of a third peak which would add to the doublet features. As a conclusion, such doublets will be considered as typical responses of NCs with tetragonal structures, whose existence was previously revealed by magneto-optical experiments.[21]

At that point, a quantitative analysis becomes possible once the expressions of the FS energy splittings are known (see ESI, Section IV). For orthorhombic crystals, we note in ascending order E_γ, E^X_{3-} and E^X_{3+} the energies of the FS bright states (see labeling in Figure 4a). The energy

splittings are connected to the electron-hole exchange interaction, *J,* and to the parameter ε, the corrective orthorhombic crystal-field term with respect to the tetragonal structure, by the following relations:

$$\Delta E' = \bar{E}_3^X - E_\gamma = J(1 - 3sin^2\theta), \text{ with } \bar{E}_3^X = (E_{3+}^X + E_{3-}^X)/2 \quad (2a)$$

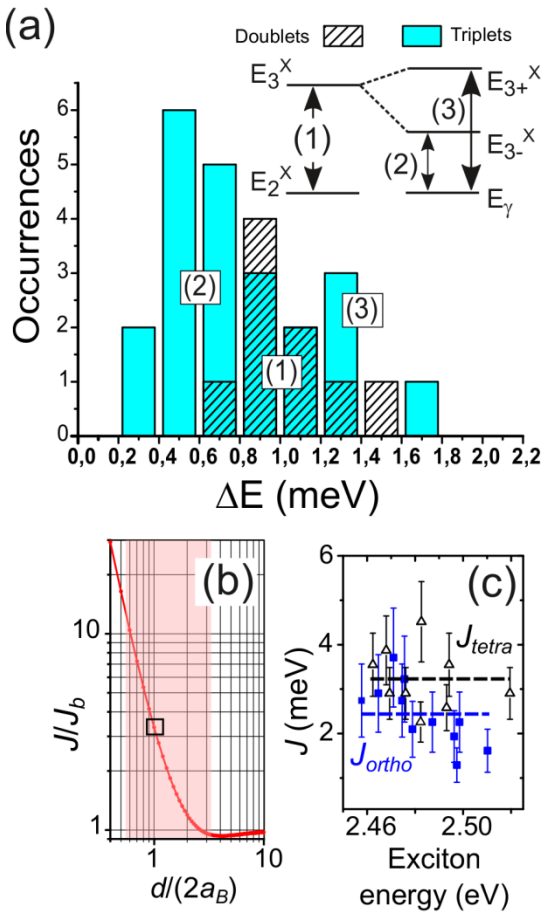

Figure 4: (a) Histogram of the energy differences reported in doublets (1) and triplets ((2) and (3)). Inset: Energy labeling of fine structure states. (b) J/J_b ratio as a function of the $d/(2a_B)$ parameter, calculated using the calculation of Romestain and Fishman.[24] The marker (open square) emphasizes the $d=2a_B$ case, and the light red region corresponds to the range spanned by the sizes present in sample 2 (see histogram in ESI*, Figure S1). (c) Value of the experimental electron-hole exchange energy as a function of the mean exciton energy, E_0: open triangles are for the tetragonal NCs, whereas solid squares refer to the orthorhombic NCs.*

$$E_{3+}^X - E_{3-}^X = \frac{4J|\varepsilon|cos^2\theta}{E_{II} - E_I}, \quad (2b)$$

where $\tan(2\theta) = \left(\frac{2\sqrt{2}\Delta_{SO}}{\Delta_{SO} - 3T}\right)$, leading to $\sin\theta = 0.48$. In Equations 2a and 2b, *J* is the only parameter which fundamentally depends on the electronic confinement. The experimental mean values of the energy splitting E^X_{3+} - E^X_{3-} = 0.55 ± 0.20 meV, and energy difference $\Delta E'$ = 0.75 ± 0.22 meV lead to *J* = 2.4 meV ± 0.7 meV and $|\varepsilon|$ = 0.08 ± 0.04 eV. We note that similar or smaller energy differences were obtained in previous studies for $CsPbBr_3$[21] and $CsPbI_3$.[44] The transition energies of the studied triplets are distributed around 2.48 eV (see ESI, Table S1), an energy which is slightly higher than the bulk lowest band-edge excitonic transition, 2.33 eV. The *J* value deduced from our experimental spectra is thus characteristic of a moderate confinement, and should noticeably deviate from the bulk value[24] (which, to our knowledge, is still unknown in $CsPbBr_3$).

Using an *ab initio* pseudopotential method, Zunger and coworkers have established a linear relationship between the inverse of a_B^3 and the bulk electron-hole exchange energy, J_b.[45] Assuming that this result can be exported to perovskite materials only if we consider the exchange

splitting originating from a hole in the lower energy split-off valence band with $S^h = \frac{1}{2}$ (to ensure consistency in the comparison with band-edge exciton in perovskite), we would obtain for $CsPbBr_3$, $J_b \approx 0.19$ meV. Such a value is known to be underestimated (by more than a factor two)[45] as compared to experimental values, but may define a lower boundary for J_b. M.A. Becker *et al.* have calculated a $J = 0.29$ meV that is close to the bulk value calculated by Zunger.[29] The ratio J/J_b can also be estimated in a model, based on the envelope function approximation, for an exciton inside a cube.[24] The original derivation, reconsidered here for an expanded range of the $d/2a_B$ parameter, leads to an enhancement $J/J_b \approx 3.3$ for $d = 2a_B$ (Figure 4b) which keeps in fair agreement with the estimation obtained by Zunger. We note that the J estimated value compares well to the value obtained in $(C_4H_9NH_3)_2PbBr_4$ quantum-wells [46] when we take into account the differences of EBEs in these two materials and under conditions where dielectric constants are of the same order. In our case, the EBE is an order of magnitude smaller than for $(C_4H_9NH_3)_2PbBr_4$, as a consequence we obtain an exchange energy an order of magnitude smaller. In a recent investigation an estimation of the exchange energy could be obtained in an hybrid bulk compound ($CH_3NH_3PbCl_xI_{3-x}$), through the analysis of time-resolved Faraday rotation (TRFR) measurements.[47] Amazingly this study places J_b in the μeV range whereas in this system the exciton Bohr diameter is slightly lower than in $CsPbBr_3$ and the EBE is of the same order.[48] Such discrepancy might thus have an extrinsic origin. For instance the excitation regime used in the TRFR experiments leads to large carrier densities with long recombination times. Screening of the Coulomb interaction may then play a decisive role and contribute to decrease J_b in a drastic manner.[20]
Furthermore, there is no clear dependence of J on the excitonic transition energy, E_0 (Figure 4c). This is essentially due to the small extent in energy of the interval probed in our experiments. A rough model indeed shows that the typical variation of 60 meV reported here for E_0 leads, in the strong-confinement limit, to a variation of 0.7 nm in the size around the 7 nm value. The effective mass model predicts that the exchange energy is enhanced by a factor proportional to $(\frac{a_B}{l})^3$, where l is the characteristic size of the NC (radius in spherical NCs or edge length in cubes).[23–25,27,28,45,49] A decrease of 0.7 nm in NC size should thus correspond to an enhancement of the J value of ≈ 30 %. Such variations are thus in the uncertainty range of our measurements especially as the scaling evidenced experimentally may follow a law with a lower power than the one fixed by the effective mass approximation.[45,50]

This study also provides a first estimation (in absolute value) of the crystal-field variation induced by the lowering of symmetry from the tetragonal to the orthorhombic structure. We moreover check that $|\varepsilon|$ is small in front of the relevant energetic quantities (see ESI) and validate the perturbation approach used in this work to derive eigenenergies corresponding to the orthorhombic band-structure energies. Consistently, this *a posteriori* also justifies that an average absorption spectrum may be used to extract the T and Δ_{SO} parameters of bulk $CsPbBr_3$ whatever the crystalline structure.

The panel of spectra retrieved in this work also allows the extraction of J for the NCs which are supposed to have a tetragonal structure. If we note here E_2^X and E_3^X the energies of the $|0_B\rangle$ and degenerate $|\pm1\rangle$ states (diagram in Figure 4a), then the energy difference E_3^X-E_2^X writes as follows [21,46]:

$$E_3^X - E_2^X = J(1 - 3sin^2\theta). \quad (3)$$

In the doublets, we find E_3^X-E_2^X = 1.0 ± 0.2 meV, and we deduce the value J = 3.2 ± 0.6 meV. The same splitting value was already measured for PL doublets detected at 2.42 eV, at 2 K, for NCs.[21] In our experiments, PL doublets were detected at ~ 5 K at energies between 2.46 eV and 2.52 eV. As in triplets, the explored domain does not allow to observe a size dependence correlated to the enhancement of the exchange energy by confinement. Finally two observations should be made in connection: first, the occurrences of the two types of excitons are energy-independent which is consistent with the fact that each crystalline structure is represented in the different NCs populations as far as size is concerned. Second, the uncertainty value that results from the available statistics seems to indicate comparable values for J in the explored structures (tetragonal and orthorhombic), as expected, considering that each set of NCs is globally characterized by the same average level of confinement.

Corollary our calculations place an optically forbidden state below the first emissive state with an energy separation $\Delta E_D \approx 1.1$ meV in the orthorhombic structure and $\Delta E_D \approx 1.5$ meV in the tetragonal one, for NC sizes comparable to the Bohr diameter. This energy separation should increase for smaller sizes. Contrary to what is observed in the more studied II-VI and III-V semiconductor NCs, the dark state does not seem to be partly allowed. This organization of the excitonic structure should thus have a strong impact on the emission properties, in particular by thermal mixing of the lower energy states in the FS.[35] The effective lifetime of the lowest energy state, $|Z\rangle$, in triplets, τ_{eff}, is measured around 80 ps at 5 K (see ESI, Figure S7). At temperature T, such that $k_BT < \Delta E_D$, the feedback effects remain weak or negligible so that τ_{eff} represents the intrinsic decay rate (including radiative and non-radiative contributions) of the $|Z\rangle$ state. Its surprisingly small value obviously raises the question of its radiative nature. Among the possible channels, transfer to the dark state is at present time the most plausible. Extensive temperature-dependent time-resolved studies are still required to probe the model and reach precise positioning of the dark state.

Let us finally emphasize that the previous considerations are valid whether the FS splitting properties are indeed determined by the mixing of carriers states resulting from spin-orbit interaction and crystal field effects. This picture comes as an alternative view on the FS splitting issue that may also be considered under the angle of the Rashba effect.[29] The latter phenomenon requires an inversion asymmetry to be operative. Actually the structural fluctuations that may cause this loss of inversion symmetry are not known and the few studies which claim they have probed a Rashba-type effect are still rare; so far they have all addressed hybrid perovskite compounds.[51] In $CsPbBr_3$ cation positional instabilities (in particular displacement of the Cs^+ cation) as well as surface effects are invoked.[29] Nevertheless, in halide based perovskite materials, movement of the halide ions may also contribute to large changes in the electronic charge distribution.[52,53] Given the very partial current state of knowledge about $CsPbBr_3$ we thus finally stress the importance to progress in the identification of the dynamical mechanisms that may trigger local electric field extending beyond the characteristic Rashba length scale.[51]

Conclusions

In summary, we carried out a quantitative study of the electronic structure of tetragonal and orthorhombic $CsPbBr_3$ NCs. From averaged absorption measurements performed in NCs which do not show confinement effects, the fundamental parameters defining the bulk band structure near the gap have been determined: the tetragonal crystal field correction with respect to the cubic crystal field, T = - 0.34 ± 0.05 eV, and spin-orbit splitting, Δ_{SO} = 1.20 ± 0.06 eV. The band–edge excitonic transition of $CsPbBr_3$ NCs with sizes close to the Bohr diameter was explored at the individual object scale through μ-PL experiments. We confirm that the excitonic FS is dominated by three bright states giving clear spectroscopic signatures with well-defined polarization properties and correlated to the crystal symmetries: doublets for tetragonal and triplets for orthorhombic crystal structures. The theoretical approach which laid the foundation of previous studies was reconsidered. That led to a quantitative estimation of the electron-hole pair exchange interaction, J, in $CsPbBr_3$ ($J \approx 3$ meV) and placed a dark state ≈ 1 meV below the first optically active state in both types of NCs. The amplitude of the correction (in absolute value) which affects the crystal field amplitude when lowering the symmetry from the tetragonal to the orthorhombic phase could also be determined ($|\varepsilon| \approx 0.08$ eV). Finally, preliminary basic analysis indicates that J is very likely enhanced by confinement in the studied NCs. We give a consistent and quantitative picture of the exciton structure in confined inorganic $CsPbBr_3$ that does not need to consider a supplementary breaking of symmetry related to the Rashba effect, as proposed in the work of M.A. Becker *et al.*.[29] All these findings are crucial to build accurate models of optoelectronic properties; they contribute to the exploration of the material potential having in view its implementation in quantum information applications,[21,44] and guide incipient studies on spin generation and manipulation.[54] More pragmatically, this work also paves the way for future studies dedicated to the localization of the dark FS state and its coupling to bright states, along with the role of increased confinement on excitonic properties.

Conflicts of interest

There are no conflicts of interest to declare.

Acknowledgements

This work has been supported by the Région Ile-de-France in the framework of DIM Nano-K and French state funds managed by the ANR within the Investissements d'Avenir program under reference ANR-11-IDEX-0004-02, and more specifically within the framework of the Cluster of Excellence MATISSE led by Sorbonne Universités. JR acknowledges Sorbonne Universités UPMC for the financial support in the framework of the project SOFISTIKITE of Emergence SU. E.L. thanks the support ERC starting grant blackQD (n°756225). We warmly thank for their technical assistances M. Bernard and F. Margaillan respectively for cryogenics and optics.

Authorship

N.G. and E.L. synthesized the NCs and achieved structural characterization; J.R., L.M.A. and L.L. performed the experimental work; V.S., L.L., C.T. and F.B. provided the theoretical support (ESI); T.B., M.C. and A.B. wrote the paper.

Notes and references

1 C. C. Stoumpos and M. G. Kanatzidis, *Acc. Chem. Res.*, 2015, **48**, 2791–2802.
2 A. Kojima, K. Teshima, Y. Shirai and T. Miyasaka, *J. Am. Chem. Soc.*, 2009, **131**, 6050–6051.
3 M. M. Lee, J. Teuscher, T. Miyasaka, T. N. Murakami and H. J. Snaith, *Science*, 2012, **338**, 643–647.
4 J. A. Sichert, Y. Tong, N. Mutz, M. Vollmer, S. Fischer, K. Z. Milowska, R. Garcia Cortadella, B. Nickel, C. Cardenas-Daw, J. K. Stolarczyk, A. S. Urban and J. Feldmann, *Nano Lett.*, 2015, **15**, 6521–6527.
5 L. Protesescu, S. Yakunin, M. I. Bodnarchuk, F. Krieg, R. Caputo, C. H. Hendon, R. X. Yang, A. Walsh and M. V. Kovalenko, *Nano Lett.*, 2015, **15**, 3692–3696.
6 S. Sun, D. Yuan, Y. Xu, A. Wang and Z. Deng, *Acs Nano*, 2016, **10**, 3648–3657.
7 Y. Xu, Q. Chen, C. Zhang, R. Wang, H. Wu, X. Zhang, G. Xing, W. W. Yu, X. Wang, Y. Zhang and M. Xiao, *J. Am. Chem. Soc.*, 2016, **138**, 3761–3768.
8 S. Gonzalez-Carrero, R. E. Galian and J. Pérez-Prieto, *Opt. Express*, 2016, **24**, A285–A301.
9 X. Li, Y. Wu, S. Zhang, B. Cai, Y. Gu, J. Song and H. Zeng, *Adv. Funct. Mater.*, 2016, **26**, 2435–2445.
10 A. Zakutayev, C. M. Caskey, A. N. Fioretti, D. S. Ginley, J. Vidal, V. Stevanovic, E. Tea and S. Lany, *J. Phys. Chem. Lett.*, 2014, **5**, 1117–1125.
11 S. Yakunin, L. Protesescu, F. Krieg, M. I. Bodnarchuk, G. Nedelcu, M. Humer, G. De Luca, M. Fiebig, W. Heiss and M. V. Kovalenko, *Nat. Commun.*, 2015, **6**, 8056.

12 G. Rainò, G. Nedelcu, L. Protesescu, M. I. Bodnarchuk, M. V. Kovalenko, R. F. Mahrt and T. Stöferle, *ACS Nano*, 2016, **10**, 2485–2490.
13 N. S. Makarov, S. Guo, O. Isaienko, W. Liu, I. Robel and V. I. Klimov, *Nano Lett.*, 2016, **16**, 2349–2362.
14 Y.-S. Park, S. Guo, N. S. Makarov and V. I. Klimov, *ACS Nano*, 2015, **9**, 10386–10393.
15 F. Hu, C. Yin, H. Zhang, C. Sun, W. W. Yu, C. Zhang, X. Wang, Y. Zhang and M. Xiao, *Nano Lett.*, 2016, **16**, 6425–6430.
16 K. Heidrich, H. Künzel and J. Treusch, *Solid State Commun.*, 1978, **25**, 887–889.
17 K. Heidrich, W. Schäfer, M. Schreiber, J. Söchtig, G. Trendel, J. Treusch, T. Grandke and H. J. Stolz, *Phys. Rev. B*, 1981, **24**, 5642–5649.
18 G. Murtaza and I. Ahmad, *Phys. B-Condens. Matter*, 2011, **406**, 3222–3229.
19 J. Even, L. Pedesseau, J.-M. Jancu and C. Katan, *J. Phys. Chem. Lett.*, 2013, **4**, 2999–3005.
20 Z. G. Yu, *Sci. Rep.*, 2016, **6**, 28576.
21 M. Fu, P. Tamarat, H. Huang, J. Even, A. L. Rogach and B. Lounis, *Nano Lett.*, 2017, 2895–2901.
22 T. Takagahara, *Phys. Rev. Lett.*, 1993, **71**, 3577–3580.
23 M. Chamarro, C. Gourdon, P. Lavallard, O. Lublinskaya and A. I. Ekimov, *Phys. Rev. B*, 1996, **53**, 1336–1342.
24 R. Romestain and G. Fishman, *Phys. Rev. B*, 1994, **49**, 1774–1781.
25 M. Nirmal, D. Norris, M. Kuno, M. Bawendi, A. Efros and M. Rosen, *Phys. Rev. Lett.*, 1995, **75**, 3728–3731.
26 A. Franceschetti and A. Zunger, *Phys. Rev. Lett.*, 1997, **78**, 915–918.
27 T. Takagahara, *Phys. Rev. B*, 2000, **62**, 16840–16855.
28 G. Bester, S. Nair and A. Zunger, *Phys. Rev. B*, 2003, **67**, 161306.
29 M. A. Becker, R. Vaxenburg, G. Nedelcu, P. C. Sercel, A. Shabaev, M. J. Mehl, J. G. Michopoulos, S. G. Lambrakos, N. Bernstein, J. L. Lyons, T. Stoferle, R. F. Mahrt, M. V. Kovalenko, D. J. Norris, G. Raino and A. L. Efros, *Nature*, 2018, **553**, 189–+.
30 S. Vezzoli, M. Manceau, G. Leménager, Q. Glorieux, E. Giacobino, L. Carbone, M. De Vittorio and A. Bramati, *ACS Nano*, 2015, **9**, 7992–8003.
31 A. J. Bennett, M. A. Pooley, R. M. Stevenson, M. B. Ward, R. B. Patel, A. B. de la Giroday, N. Skoeld, I. Farrer, C. A. Nicoll, D. A. Ritchie and A. J. Shields, *Nat. Phys.*, 2010, **6**, 947–950.
32 K. Mueller, T. Kaldewey, R. Ripszam, J. S. Wildmann, A. Bechtold, M. Bichler, G. Koblmueller, G. Abstreiter and J. J. Finley, *Sci. Rep.*, 2013, **3**, 1906.
33 M. Ghali, K. Ohtani, Y. Ohno and H. Ohno, *Nat. Commun.*, 2012, **3**, 661.
34 R. M. Stevenson, R. J. Young, P. Atkinson, K. Cooper, D. A. Ritchie and A. J. Shields, *Nature*, 2006, **439**, 179–182.
35 O. Labeau, P. Tamarat and B. Lounis, *Phys. Rev. Lett.*, 2003, **90**, 257404.
36 M. Sebastian, J. A. Peters, C. C. Stoumpos, J. Im, S. S. Kostina, Z. Liu, M. G. Kanatzidis, A. J. Freeman and B. W. Wessels, *Phys. Rev. B*, 2015, **92**, 235210.
37 J. Li, X. Yuan, P. Jing, J. Li, M. Wei, J. Hua, J. Zhao and L. Tian, *RSC Adv*, 2016, **6**, 78311–78316.
38 A. D. Wright, C. Verdi, R. L. Milot, G. E. Eperon, M. A. Pérez-Osorio, H. J. Snaith, F. Giustino, M. B. Johnston and L. M. Herz, *Nat. Commun.*, 2016, **7**, 11755.
39 J. Even, L. Pedesseau, J.-M. Jancu and C. Katan, *Phys. Status Solidi-Rapid Res. Lett.*, 2014, **8**, 31–35.
40 F. Hu, H. Zhang, C. Sun, C. Yin, B. Lv, C. Zhang, W. W. Yu, X. Wang, Y. Zhang and M. Xiao, *Acs Nano*, 2015, **9**, 12410–12416.
41 M. C. Brennan, J. E. Herr, T. S. Nguyen-Beck, J. Zinna, S. Draguta, S. Rouvimov, J. Parkhill and M. Kuno, *J. Am. Chem. Soc.*, 2017, **139**, 12201–12208.
42 S. Hirotsu, J. Harada, M. Iizumi and K. Gesi, *J. Phys. Soc. Jpn.*, 1974, **37**, 1393–1398.
43 M. Rodova, J. Brozek, K. Knizek and K. Nitsch, *J. Therm. Anal. Calorim.*, 2003, **71**, 667–673.
44 C. Yin, L. Chen, N. Song, Y. Lv, F. Hu, C. Sun, W. W. Yu, C. Zhang, X. Wang, Y. Zhang and M. Xiao, *Phys. Rev. Lett.*, , DOI:10.1103/PhysRevLett.119.026401.
45 H. X. Fu, L. W. Wang and A. Zunger, *Phys. Rev. B*, 1999, **59**, 5568–5574.
46 K. Tanaka, T. Takahashi, T. Kondo, K. Umeda, K. Ema, T. Umebayashi, K. Asai, K. Uchida and N. Miura, *Jpn. J. Appl. Phys.*, 2005, **44**, 5923–5932.
47 P. Odenthal, W. Talmadge, N. Gundlach, R. Wang, C. Zhang, D. Sun, Z.-G. Yu, Z. V. Vardeny and Y. S. Li, *Nat. Phys.*, 2017, **13**, 894–+.

48 K. Tanaka, T. Takahashi, T. Ban, T. Kondo, K. Uchida and N. Miura, *Solid State Commun.*, 2003, **127**, 619–623.
49 M. Chamarro, C. Gourdon, P. Lavallard, O. Lublinskaya and A. I. Ekimov, *Il Nuovo Cimento D*, 1995, **17**, 1407–1412.
50 U. Banin, J. C. Lee, A. A. Guzelian, A. V. Kadavanich and A. P. Alivisatos, *Superlattices Microstruct.*, 1997, **22**, 559–567.
51 E. Mosconi, T. Etienne and F. De Angelis, *J. Phys. Chem. Lett.*, 2017, **8**, 2247–2252.
52 C. Eames, J. M. Frost, P. R. F. Barnes, B. C. O'Regan, A. Walsh and M. S. Islam, *Nat. Commun.*, 2015, **6**, 7497.
53 Z. Xiao, Y. Yuan, Y. Shao, Q. Wang, Q. Dong, C. Bi, P. Sharma, A. Gruverman and J. Huang, *Nat. Mater.*, 2015, **14**, 193–198.
54 D. Canneson, E. V. Shornikova, D. R. Yakovlev, T. Rogge, A. A. Mitioglu, M. V. Ballottin, P. C. M. Christianen, E. Lhuillier, M. Bayer and L. Biadala, *Nano Lett.*, 2017, **17**, 6177–6183.